eScience 3 (2023) 100175

Contents lists available at ScienceDirect

eScience

journal homepage: www.keaipublishing.com/en/journals/escience

Research Paper

Enhanced room-temperature Na^+ ionic conductivity in $Na_{4.92}Y_{0.92}Zr_{0.08}Si_4O_{12}$

Aikai Yang [a,b], Kai Yao [a], Mareen Schaller [c], Enkhtsetseg Dashjav [a], Hang Li [c], Shuo Zhao [d], Qiu Zhang [d], Martin Etter [e], Xingchen Shen [f], Huimin Song [g], Qiongqiong Lu [h], Ruijie Ye [a], Igor Moudrakovski [i], Quanquan Pang [g], Sylvio Indris [c,*], Xingchao Wang [j,*], Qianli Ma [a,*], Frank Tietz [a,k], Jun Chen [d,*], Olivier Guillon [a,b,k,l]

[a] Forschungszentrum Jülich GmbH, Institute of Energy and Climate Research, Materials Synthesis and Processing (IEK-1), 52425 Jülich, Germany
[b] Institute of Mineral Engineering (GHI), RWTH Aachen University, Forckenbeckstraße 33, 52074 Aachen, Germany
[c] Institute for Applied Materials-Energy Storage Systems (IAM-ESS), Karlsruhe Institute of Technology (KIT), 76344 Eggenstein-Leopoldshafen, Germany
[d] Renewable Energy Conversion and Storage Center (RECAST), Haihe Laboratory of Sustainable Chemical Transformations, Key Laboratory of Advanced Energy Materials Chemistry (Ministry of Education), College of Chemistry, Nankai University, Tianjin 300071, China
[e] Deutsches Elektronen-Synchrotron (DESY), Notkestrasse 85, 22607 Hamburg, Germany
[f] Laboratoire de Cristallographie et Sciences des Matériaux (CRISMAT), CNRS, ENSICAEN, 14000 Caen, France
[g] Beijing Key Laboratory of Theory and Technology for Advanced Batteries Materials, School of Materials Science and Engineering, Peking University, Beijing 100871, China
[h] Institute of Materials, Henan Academy of Sciences, Henan Key Laboratory of Advanced Conductor Materials, Zhengzhou 450046, China
[i] Max Planck Institute for Solid State Research, Heisenbergstraße 1, 70569 Stuttgart, Germany
[j] State Key Laboratory of Chemistry and Utilization of Carbon Based Energy Resources, Key Laboratory of Advanced Functional Materials, Autonomous Region, Institute of Applied Chemistry, College of Chemistry, Xinjiang University, Urumqi, Xinjiang 830046, China
[k] Forschungszentrum Jülich GmbH, Helmholtz Institute Münster (IEK-12), 52425 Jülich, Germany
[l] Jülich Aachen Research Alliance, JARA-Energy, 52425 Jülich, Germany

HIGHLIGHTS

- Novel composition $Na_{4.92}Y_{0.92}Zr_{0.08}Si_4O_{12}$ (NYZS) exhibits high bulk and total conductivities of up to 6.5 and 3.3 mS cm^{-1}, respectively.
- NYZS shows an ultra-wide electrochemical window of >10 V (*vs.* Na^+/Na) and a high critical current density of 2.4 mA cm^{-2}.
- A synergistic effect of increased vacancies and an improved chemical environment contributes to high conductivity.

GRAPHICAL ABSTRACT

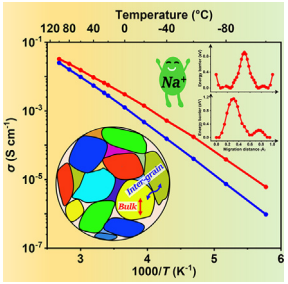

ARTICLE INFO

Keywords:
Solid-state electrolytes
Sodium superionic conductors
$Na_{4.92}Y_{0.92}Zr_{0.08}Si_4O_{12}$
High conductivity
Ultra-wide electrochemical window

ABSTRACT

Developing cost-effective and reliable solid-state sodium batteries with superior performance is crucial for stationary energy storage. A key component in facilitating their application is a solid-state electrolyte with high conductivity and stability. Herein, we employed aliovalent cation substitution to enhance ionic conductivity while preserving the crystal structure. Optimized substitution of Y^{3+} with Zr^{4+} in $Na_5YSi_4O_{12}$ introduced Na^+ ion vacancies, resulting in high bulk and total conductivities of up to 6.5 and 3.3 mS cm^{-1}, respectively, at room

* Corresponding authors.
E-mail addresses: sylvio.indris@kit.edu (S. Indris), xcwang@xju.edu.cn (X. Wang), q.ma@fz-juelich.de (Q. Ma), chenabc@nankai.edu.cn (J. Chen).

https://doi.org/10.1016/j.esci.2023.100175
Received 7 June 2023; Received in revised form 1 August 2023; Accepted 4 August 2023
Available online 7 August 2023

temperature with the composition $Na_{4.92}Y_{0.92}Zr_{0.08}Si_4O_{12}$ (NYZS). NYZS shows exceptional electrochemical stability (up to 10 V *vs.* Na^+/Na), favorable interfacial compatibility with Na, and an excellent critical current density of 2.4 mA cm^{-2}. The enhanced conductivity of Na^+ ions in NYZS was elucidated using solid-state nuclear magnetic resonance techniques and theoretical simulations, revealing two migration routes facilitated by the synergistic effect of increased Na^+ ion vacancies and improved chemical environment due to Zr^{4+} substitution. NYZS extends the list of suitable solid-state electrolytes and enables the facile synthesis of stable, low-cost Na^+ ion silicate electrolytes.

1. Introduction

High-performance rechargeable batteries, such as lithium-ion batteries (LIBs), are making society more mobile, transportable and diversifying the sources of energy [1–3]. However, the escalating demand and geographical disparities of lithium and cathodes with transition metals, like nickel and cobalt, are driving up rapidly the cost of these elements [4,5]. As a potentially affordable and safe complementarity to LIBs, solid-state sodium batteries (SSSBs) offer significant resources and cost advantages [6] over conventional LIBs for grid-scale energy storage plants [7–9]. However, the implementation of solid-state batteries (SSBs) is primarily handicapped by the challenging fabrication of solid-state electrolytes (SSEs) with high ionic conductivity, good stability and the delicate preparation of optimized interfaces [10,11].

Extensive research has focused on ceramic electrolytes (sulfides and oxides) [12–14] and composite electrolytes (polymeric matrix with inorganic fillers) [15] to meet the requirements of conductivity and stability. Sulfide electrolytes (e.g., Na_3PS_4, $Na_7P_3S_{11}$) exhibit fair conductivity and compatibility with electrodes but suffer from poor chemical stability against oxygen and moisture [16]. Oxide electrolytes (e.g., β/β''-Al_2O_3, NASICON) [13,17] offer better stability and decent ionic conductivity but require high sintering temperatures [18]. β-Al_2O_3, the pioneering solid-state Na^+ ionic conductor, necessitates high sintering temperatures ranging from 1350 to 1700 °C, albeit exhibiting an impressive ionic conductivity of up to 6 mS cm^{-1} at room temperature (RT) [17]. NASICON-type SSEs ($Na_{1+x}Zr_2Si_xP_{3-x}O_{12}$, $0 \le x \le 3$), first reported by Hong *et al.* in 1976 [19], have been widely studied in structural modifications and electrochemical properties [20]. However, the easy reduction of pentavalent phosphate in NASICON limits the choice of matching cathodes with high potential. Composite electrolytes, despite facilitating favorable electrode/electrolyte interfaces, suffer from inherent poor conductivities of the polymer electrolytes and the imperative of elevated operating temperature.

Alongside the discovery of NASICON, another Na^+ ionic conductor, $Na_5YSi_4O_{12}$ (NYS), was reported by Maksimov [21], Shannon [22] and Beyeler *et al.* [23] in the 1970s. The crystal structure determination of NYS revealed almost 3 out of 7 Na^+ ions per formula unit to be highly mobile, located between stacked $Si_{12}O_{36}$ rings separated by YO_6 octahedra, contributing to its high conductivity [14,24]. NYS exhibits a reported total conductivity of $\sigma_{total\text{-}RT}$ = 1.0–1.5 mS cm^{-1} at RT [14,24,25] and $\sigma_{total\text{-}300\,°C}$ = 0.1–0.5 S cm^{-1} at 300 °C. Moreover, NYS demonstrates stability against valence change, allowing for a wide electrochemical stability window when used with Na metal as an anode [24]. Despite being discovered over forty years ago, there has been a scarcity of relevant studies on structural analysis and transport pathways for this promising and cost-effective solid-state electrolyte (SSE).

In this study, the silicate electrolyte with the composition of $Na_{4.92}Y_{0.92}Zr_{0.08}Si_4O_{12}$ (NYZS) was synthesized by a facile solid-state reaction method, in which the strategy of defect chemistry by the aliovalent substitution of Y^{3+} with Zr^{4+} introduced more Na^+ ion vacancies and regulated the concentration of defects (Kröger-Vink notation in Eq. (1)):

$$Na_{Na}^{\times} + Y_Y^{\times} \rightarrow V_{Na}^{'} + Zr_Y^{\bullet} \quad (1)$$

where the notation of $\times$, $^{\cdot}$ and $'$ represent the neutral, positive and negative net charge, respectively, and V denotes vacancies. It enables bulk conductivity at RT $\sigma_{bulk\text{-}RT}$ and total conductivity at RT $\sigma_{total\text{-}RT}$ up to 6.5 and 3.3 mS cm^{-1}, respectively. To the best of our knowledge, this (3.3 mS cm^{-1}) is the highest conductivity among NYS-type electrolytes. NYZS exhibits wide electrochemical stability of over 10 V *vs.* Na^+/Na. The excellent cycling performance, interfacial compatibility and critical current density (CCD) are also investigated. The crystal structure of NYZS and the migration pathways of Na^+ ions are elucidated by a combination of synchrotron X-ray diffraction (SYXRD) and magic-angle spinning nuclear magnetic resonance (MAS NMR) techniques together with theoretical simulations.

2. Results and discussion

2.1. Synthesis and structural analysis of NYZS

As shown in Fig. 1a, the facile solid-state reaction method was employed to synthesize the series $Na_{5-x}Y_{1-x}Zr_xSi_4O_{12}$ ($0 \le x \le 1$), which provides the feasibility of large-scale preparation of inexpensive silicate electrolytes. The corresponding XRD patterns, analysis of secondary phases, and $\sigma_{total\text{-}RT}$ of this series in dependence on Zr substitution are shown in Supplementary Figs. S1, S2 and Table S1, in which the highest $\sigma_{total\text{-}RT}$ (3.3 mS cm^{-1}) was achieved with x = 0.08, i.e., $Na_{4.92}Y_{0.92}Zr_{0.08}Si_4O_{12}$ (NYZS). The Rietveld-refined SYXRD pattern of NYZS, shown in Fig. 1b, confirmed the rhombohedral structure with $R\bar{3}c$ symmetry (Fig. 1c) as known from NYS. The refined lattice parameters are a = 21.99 Å, c = 12.61 Å, and V = 5286.1 $Å^3$. The staggered [SiO_4] tetrahedra form the 12-membered silicate rings [$Si_{12}O_{36}$] and are then stacked as columns by sharing O atoms which, in turn, are linked to each other by [YO_6] or [ZrO_6] octahedra. The combination of these rings, columns and octahedra results in a framework structure with two three-dimensionally (3D) linked channels. One of the channels is surrounded only by [SiO_4] tetrahedra and is filled by Na^+ ions on three different sites (denoted as Na1, Na2, and Na3), which are stacked to a prismatic column parallel to the c axis. Refinement of occupancy parameters of these three Na^+ ions tended to full occupancies, which indicated the immobility of these Na^+ ions in the rigid prismatic columns. Another channel is surrounded by [SiO_4] tetrahedra and [(Y, Zr)O_6] octahedra and partially occupied by Na^+ ions in two sites (denoted as Na5, Na6) forming a zigzag chain parallel to the c axis. Because of their very short interatomic distances of 1–2 Å between two Na^+ ions, a restriction in the refinement was employed to obtain equivalent isotropic atomic displacement parameters (ADPs). Their occupancies were refined freely with a restriction of a fixed sum of ions to keep the charges balanced. Zigzag chains are interconnected through Na^+ ions in Na4 sites linking the Na^+ ions on Na5 and Na6 in different channels and leading to a 3D substructure of the Na^+ ions. The Na4 sites are located near the screw axes similar and close to the Y^{3+} ions. The Na4 sites are fully occupied and reveal large apparent ADPs, indicating their high mobility. In contrast, the ADPs of Na1 sites are much smaller than those of Na4 sites. The atomic parameters of the refined structure of NYZS and the selected interatomic distances are shown in Supplementary Tables S2 and S3, respectively.

The sintered NYZS pellet is closely packed by micron-sized grains in a disordered manner. The grain size distribution is relatively narrow with 1–5 μm (Fig. 1d). The cross-sectional view (Supplementary Fig. S3) and energy dispersive X-ray (EDX) mapping analysis (Supplementary Fig. S4) exhibit pore-free morphology, dense microstructure (> 95% relative density; 2.85 g cm^{-3} of crystallographic density) and uniform elemental

distribution of NYZS, which endow its high $\sigma_{total\text{-}RT}$. The high-resolution transmission electron microscopic (HRTEM) image (Fig. 1e) of NYZS further verifies the polycrystallinity with different orientations of lattice fringes within a single grain.

X-ray photoelectron spectroscopy (XPS) is used to prove and detect the impact of the Zr incorporation in NYZS. The intensity of Zr in the survey spectra of NYZS (Supplementary Fig. S5) is not noticeable due to the low content. The binding energy of Y 3*d* (Fig. 1f), Si 2*p* (Fig. 1g) and O 1*s* (Fig. 1h) slightly shifted to higher energy (Supplementary Table S4) in NYZS compared with NYS, which is explained by the enhanced bond strength due to the shortened bond length (Supplementary Table S5). Another indication is the slight shrinkage of the *a* and *c* axis of the unit cell for NYZS (Supplementary Table S2) resulting from the smaller ionic radius of Zr^{4+}, which generally increases the binding energies.

Good stability in ambient air is crucial for synthesis, storage and subsequent processing. The XRD patterns (Supplementary Fig. S6) and Zr 3*d* XPS spectra (Fig. 1i) of the fresh and long-term exposed sample in air for three months were individually analyzed to detect any evolution of NYZS characteristics. Still, both methods show negligible changes after the storage period, which confirms the good chemical stability thanks to

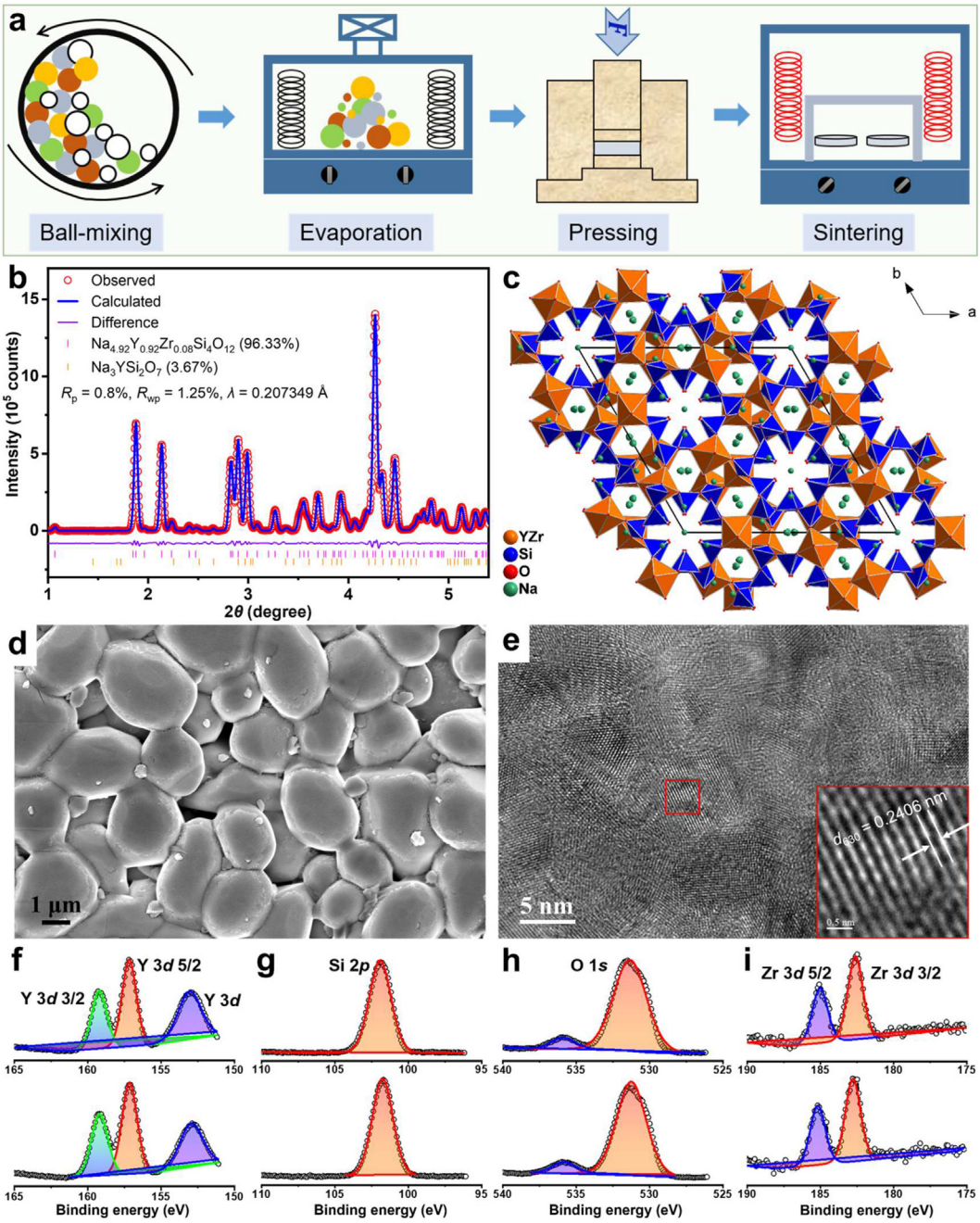

Fig. 1. Synthesis and structural analysis of NYZS. (a) Schematic of the solid-state synthesis process, which consists of ball-mixing, solvent evaporation, powder pressing and sintering. (b) Rietveld refinement against the synchrotron XRD pattern, revealing the phase purity of NYZS up to 96.33% and the secondary phase $Na_3YSi_2O_7$ of 3.67%. (c) The projection of the unit cell after Rietveld refinement viewed along the *c* axis: SiO_4 tetrahedra in blue; (Y, Zr)O_6 octahedra in brown; O atoms in red and Na atoms in green. (d) Scanning electron microscopic (SEM) image of the surface morphology of a sintered NYZS pellet with dense packing of the grains. (e) HRTEM image of NYZS showing the polycrystallinity of the grains. The inset is the magnification of the selected area, showing the clear lattice fringe of crystal facets [630]. The fitted X-ray photoelectron spectra (XPS) of (f) Y 3*d*, (g) Si 2*p* and (h) O 1*s*. The bottom and top spectra belong to NYS and NYZS, respectively. (i) The fitted XPS spectra of Zr 3*d* directly after sample preparation (bottom) and after three months (top) in ambient atmosphere.

the intrinsic stability of silicates. More importantly, the $\sigma_{\text{total-RT}}$ of NYZS did not show a significant degradation from 3.3 to 3.2 mS cm^{-1} after slightly polishing both sides of the pellet (Nyquist plots are shown in Supplementary Fig. S7). The temperature-dependent XRD patterns show no phase transition between RT and 1000 °C (Supplementary Fig. S8a). From the thermal expansion of the crystal lattice, the mean coefficient of thermal expansion (CTE) was determined ($\alpha_V = 7.0 \times 10^{-6}$ K^{-1}) based on the unit cell volume of NYZS using the length changes along the *a* and *c* axis (Supplementary Fig. S8b).

2.2. Electrical and electrochemical properties of NYZS

The electrochemical impedance spectra (EIS, Fig. 2a) with a wide frequency range from 3 GHz to 1 Hz at RT were analyzed using gold as

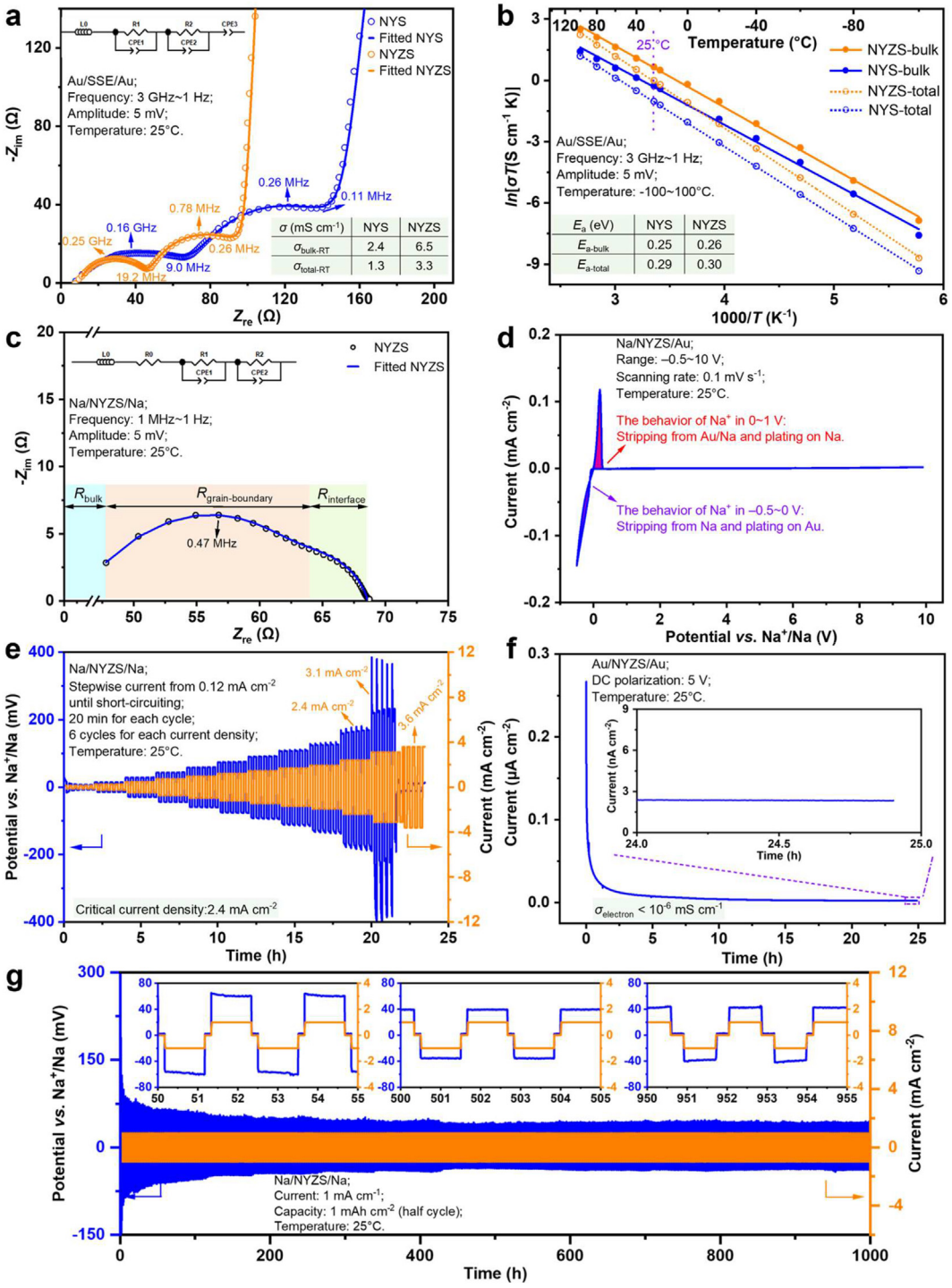

Fig. 2. Electrochemical performance of NYZS. (a) Nyquist plots of NYS and NYZS (inset: equivalent circuit for fitting). (b) Arrhenius plots of NYS and NYZS in the temperature range of ±100 °C. (c) Nyquist plot of NYZS with Na metal as electrodes (inset: equivalent circuit for fitting), revealing a low $R_{\text{interface}}$ between NYZS and Na metal. (d) Cyclic voltammetry (CV) curve of NYZS in the scanning range of −0.5 to 10 V *vs.* Na$^+$/Na with the rate of 0.1 mV s^{-1}. (e) Critical current density measurement against Na for testing the occurrence of Na metal dendrites with increasing current density until short-circuiting. (f) DC polarization curve during potentiostatic test for the electronic conductivity measurement. The inset is the magnified current curve. (g) Galvanostatic cycling measurement at the current density of 1 mA cm^{-2} and the deposition capacity of 1 mAh cm^{-2} of NYZS. The insets are the magnified curves at different periods.

blocking electrodes to distinguish the resistivity from bulk (i.e., grains) and grain boundaries. The EIS curves exhibit two consecutive semicircles in different frequency regions. The fitted values for each element in the equivalent circuit are listed in Supplementary Table S6. The first semicircle corresponds to the bulk resistance (R_{bulk}) of 46 Ω of the ceramic NYZS pellet, equivalent to the $\sigma_{bulk\text{-}RT}$ of 6.5 mS cm^{-1}. A capacitance of 1.9×10^{-12} F (capacitance of constant phase element, CPE1) and the frequency region of 3 GHz–200 MHz for the first semicircle verify this assumption [26]. The second semicircle at lower frequencies is ascribed to the ionic transport resistance of grain boundaries (R_{gb}) of 45 Ω, in which the CPE2 exhibits the capacitance of 2.1×10^{-8} F, indicating a justified assignment to the ionic migration through the grain boundaries. The nearly vertical line at low frequencies is related to the electrode contact resistance of the Au/SSE interface ($R_{interface}$), which is also verified from the magnitude of the capacitance values of 1.0×10^{-7} F. The $\sigma_{total\text{-}RT}$ of NYZS is determined by the summation of the resistance from bulk and grain boundary components, which is 3.3 mS cm^{-1} and is comparable to that of β''-alumina and NASICON. In comparison, the fitted conductivity values of the NYS sample are 2.4 ($\sigma_{bulk\text{-}RT}$) and 1.3 ($\sigma_{total\text{-}RT}$) mS cm^{-1}, which are both inferior to those of NYZS. Oxide-based SSEs usually exhibit high R_{gb} [27], but here R_{gb} is similar to R_{bulk}, which is one of the advantages of NYS and NYZS.

Temperature-dependent Na^+ ionic conductivities of NYS and NYZS samples were measured between −100 and 100 °C and plotted as Arrhenius curves (Fig. 2b). Determined from the Arrhenius plot, the activation energies of bulk ($E_{a\text{-}bulk}$) and total conductivity ($E_{a\text{-}total}$) of NYZS are 0.26 and 0.30 eV, respectively. The E_a values of NYS are comparable with those of NYZS, which are 0.25 ($E_{a\text{-}bulk}$) and 0.29 eV ($E_{a\text{-}total}$). The details of the calculation and comparison of E_a are exhibited in Supplementary Tables S7 and S8.

The interfacial compatibility between Na metal and NYZS was evaluated by the magnitude of the $R_{interface}$ against Na metal and the cyclic voltammetry (CV) test. Benefiting from the excellent ductility of Na metal and chemically stable contacting interface, the intrinsic $R_{interface}$ is only 4 Ω cm^2 (Fig. 2c) in the Na/NYZS/Na symmetric cell, which is lower than most values of the published Na^+ and Li^+ solid-state conductors [11]. Values of the fitted equivalent circuit parameters of the symmetric Na/NYZS/Na cells are listed in Supplementary Table S9.

The CV curve (Fig. 2d) was also tested with a Na/NYZS/Au cell in the scanning range from −0.5 to 10 V *vs.* the Na^+/Na electrode. The reduction peak (−0.5 to 0 V) and the oxidation peak (0–0.5 V) were induced by the stripping and plating of Na^+ ions at the Na/NYZS interfaces, respectively. A couple of symmetric redox peaks with nearly the same area suggest high reversibility of Na metal and no side reactions between NYZS and Na. The absence of significant oxidation peaks observed in the voltage range from 0.5 to 10 V implies that NYZS has a wide electrochemical window of up to 10 V, which is comparable with other oxide-based SSEs [28]. To be able to fairly evaluate the electrochemical stability window of NYZS, in addition to the CV measurement under the Na/NYZS/Au cell configuration, another two testing methodologies have been adopted to amplify the potentially invisible electrochemical response [28–30]. Fine NYZS powder along with conductive carbon Super P was fabricated into electrodes and examined by CV curves and (dis)charge performance in liquid and solid-state cells, respectively. Despite the sufficient contact area between NYZS and Super P, NYZS exhibited neither decomposition nor side-reaction during the measured intervals. Detailed results and analyses are presented in Supplementary Fig. S9 and its Notes. These robust proofs emphasize the superiority of NYZS in terms of its ultra-wide electrochemical stability. Matching NYZS with high-potential cathodes to take advantage of its ultra-wide electrochemical window requires further investigation.

The CCD of the NYZS pellet is observed at 2.4 mA cm^{-2} (Fig. 2e), which is ascribed to the dense microstructure, high ionic conductivity and superior interfacial compatibility. When the applied current density reaches 3.1 mA cm^{-2}, the polarization voltage becomes unstable and shows large voltage spikes, indicating that the interface between Na and NYZS starts to deteriorate, which gives rise to uneven current distribution and further short-circuiting at 3.6 mA cm^{-2}.

The DC polarization curve under potentiostatic test using Au as blocking electrodes shows negligible electronic conductivity ($\sigma_{electron}$) of below 10^{-6} mS cm^{-1} (Fig. 2f). Therefore, the corresponding Na^+ ionic transference number t_{Na^+} is 1.0 in NYZS, indicating the good ionic conducting and electronic insulating properties [31].

The galvanostatic cycling performance was tested in a symmetric Na/NYZS/Na pouch cell (see Supplementary Fig. S10), applying a constant pressure of ~50 MPa. As shown in Fig. 2g, the steady cycling can be carried out for more than 1000 h without significant voltage fluctuations at the current density of 1 mA cm^{-2} and the deposition capacity of 1 mAh cm^{-2} for a half cycle. The polarization voltage gradually decreases within the first 100 h, which is attributed to the improved contact area during the redistribution of Na^+ ions under pressure, thus reducing the $R_{interface}$. The following decreased polarization voltage in the cycling process is dictated by the slight Na dendritic formation (supposed "soft breakdown" before reaching short-circuit) from both sides of the pellet [32], which can be verified by post-test analysis of EIS and optical inspection (Supplementary Figs. S11 and S12) of the short-circuited cell.

2.3. Analysis of chemical environment with NMR spectroscopy

The ^{23}Na NMR spectra for NYS and NYZS display a sharp peak at ~14 ppm and broad overlapping signals between −30 and 8 ppm in Supplementary Fig. S13. Due to the strong second-order quadrupolar interaction of the sodium nuclei, the broadening of the resonance cannot be completely averaged with MAS and thus remains unresolved in these 1D spectra. The ^{29}Si MAS spectra (Supplementary Fig. S14) for both samples show two resonance peaks at −80.4 and −85.3 ppm representing the two different Si sites, as derived from the structural analysis. The splitting of both resonances in the spectrum of NYS indicates different local environments caused by partially unoccupied neighboring Na sites. In the NYZS sample, this spitting is not observed, revealing a higher degree of local disorder surrounding the [SiO_4] tetrahedra induced by the incorporation of Zr into the crystal lattice. This also results in an additional resonance at −87.6 ppm, which is assigned to Zr next nearest neighbor around Na. The ^{89}Y MAS NMR spectra (Supplementary Fig. S15) for both samples show only a single resonance at 267.5 ppm, consistent with the single Y site in this crystal structure. Again, a line broadening observed for NYZS in comparison to NYS indicates a higher degree of structural disorder caused by Zr in the lattice.

Due to the multiple overlapping signals observed in the 1D ^{23}Na MAS NMR spectra, additional ^{23}Na multi-quantum (MQ) MAS NMR experiments were performed. The results are shown in Figs. 3a (NYS) and b (NYZS), which allow the separation of the isotropic and anisotropic contributions for half-integer quadrupolar sodium nuclei. The narrow resonance at 14 ppm, which was detected for both samples in the ^{23}Na 1D MAS spectra, is labeled with "A". The broad resonance, as displayed in Supplementary Fig. S12, can be separated into a narrower peak at approximately 6 ppm (labeled with "B") and a broad contribution (labeled with "C"). The NYS sample shows an additional resonance labeled with "D" that was not detected for NYZS. We, therefore, assign this peak to one of the partially occupied Na sites in the crystal structure of NYS that is emptied in NYZS due to the aliovalent substitution of Zr^{4+} for Y^{3+}, as also expressed in the lower Na content per formula unit. The higher amount of vacancies of Na sites facilitate the Na^+ ion diffusion in NYZS.

The temperature-dependent static ^{23}Na NMR spectra were acquired between 260 and 595 K for both samples. The line shapes for the NYS sample are shown in Supplementary Fig. S16a. The spectra contain a broad line with a full width at half maximum (FWHM) of 7.4 kHz at 260 K and the peaks become narrower and are shifted to lower ppm values above 400 K. Additionally, a shoulder at the right side of the resonance is formed. At elevated temperatures, the faster motion of the Na^+ ions (with jump rates faster than the static FWHM) results in an averaging of the

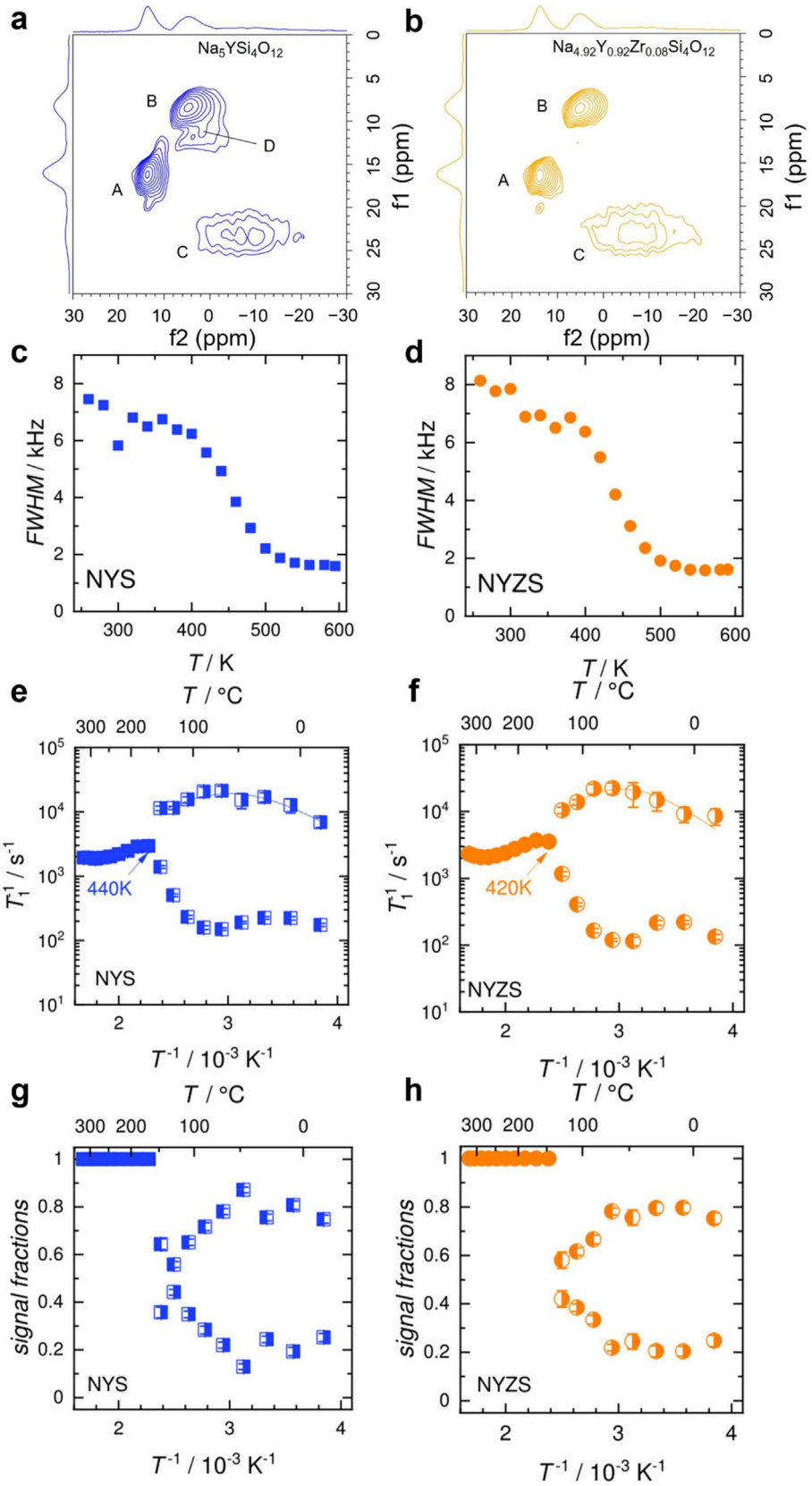

Fig. 3. Comparison and analysis of NMR results for both NYS and NYZS. The 2D ^{23}Na MQ MAS NMR spectra of (a) NYS and (b) NYZS. The different contributions are labeled with "A", "B", "C" and "D". Temperature-dependent static ^{23}Na NMR linewidths (full width at half maximum, FWHM) for (c) NYS and (d) NYZS (cf. Fig. S13). (e–h) Static ^{23}Na relaxometry: temperature-dependent relaxation rates T_1^{-1} for (e) NYS and (f) NYZS; the corresponding signal fractions in the magnetization transients of (g) NYS and (h) NYZS.

local sodium environments and causes the motional narrowing of the line shapes. The FWHM decreases to ~1.6 kHz at 595 K. The temperature-dependent results of NYZS also display a shift to lower ppm of the resonance as well as motional narrowing at elevated temperature (Supplementary Fig. S16b). For the NYS and the NYZS samples, the motional narrowing starts at 400 K and 320 K, respectively, and the corresponding temperature-dependent FWHM are shown in Figs. 3c and d.

The local hopping of the Na^+ ions was investigated by determining the relaxation times T_1 using an inversion recovery pulse sequence. These relaxation times are sensitive to motions on time scales τ of the order of the inverse Larmor frequency ($\omega_L^{-1} \approx$ few ns). The temperature dependence of the relaxation rate T_1^{-1} according to the Bloembergen-Purcell-Pound theory (BPP theory) is given by

$$T_1^{-1} \sim \left(\frac{\tau}{1+\omega_L^2\tau^2} + \frac{4\tau}{1+4\omega_L^2\tau^2}\right) \quad (2)$$

$$\text{with } \tau^{-1} = \tau_0^{-1} \cdot \exp\left(\frac{-E_a}{k_B T}\right) \quad (3)$$

where E_a is the activation energy, k_B is the Boltzmann constant, T is the thermodynamic temperature and τ is the correlation time which can be associated with the average residence time of the Na^+ ions. Their hopping rate is given by the inverse residence time.

The temperature-dependent results of the relaxation rates T_1^{-1} are shown in Figs. 3e (NYS) and f (NYZS). Both samples show a rather similar trend in their relaxation rates. Starting at the lowest temperature (260 K), two different relaxation rates are detected, which can be understood as two different types of Na^+ ions with different hopping rates and, thus also, diffusion pathways and mobility.

The corresponding signal fractions are shown in Figs. 3g (NYS) and h (NYZS). The faster relaxation rates of NYS and NYZS have a signal fraction of approximately 20–25% below 360 K. Above this temperature, the signal fractions approach roughly a 50% distribution until 440 and 420 K, respectively. The difference between both relaxation rates decreases in the same temperature range. Above 440 K, only one relaxation rate is detectable, and thus all Na^+ ions have enough energy to use the favored (faster) diffusion pathway. Therefore, all Na^+ ions can equally diffuse along both diffusion pathways above this temperature. From the static ^{23}Na relaxometry and line shape analysis, the two distinct migration pathways for Na^+ ions in NYS and NYZS are visible from the experimental perspective.

The faster relaxation rates for both samples can be fitted with BPP and Arrhenius equations (Eqs. (2) and (3)) in the temperature range from 260 to 420 or 460 K, yielding the temperature-dependent average hopping rate of the Na^+ ions as well as the activation energy E_a. E_a is (0.18 ± 0.02) eV for NYS and (0.23 ± 0.03) eV for NYZS. The average hopping rates τ^{-1} at 298 K are 2.6×10^8 and 2.3×10^8 s^{-1} for NYS and NYZS, respectively.

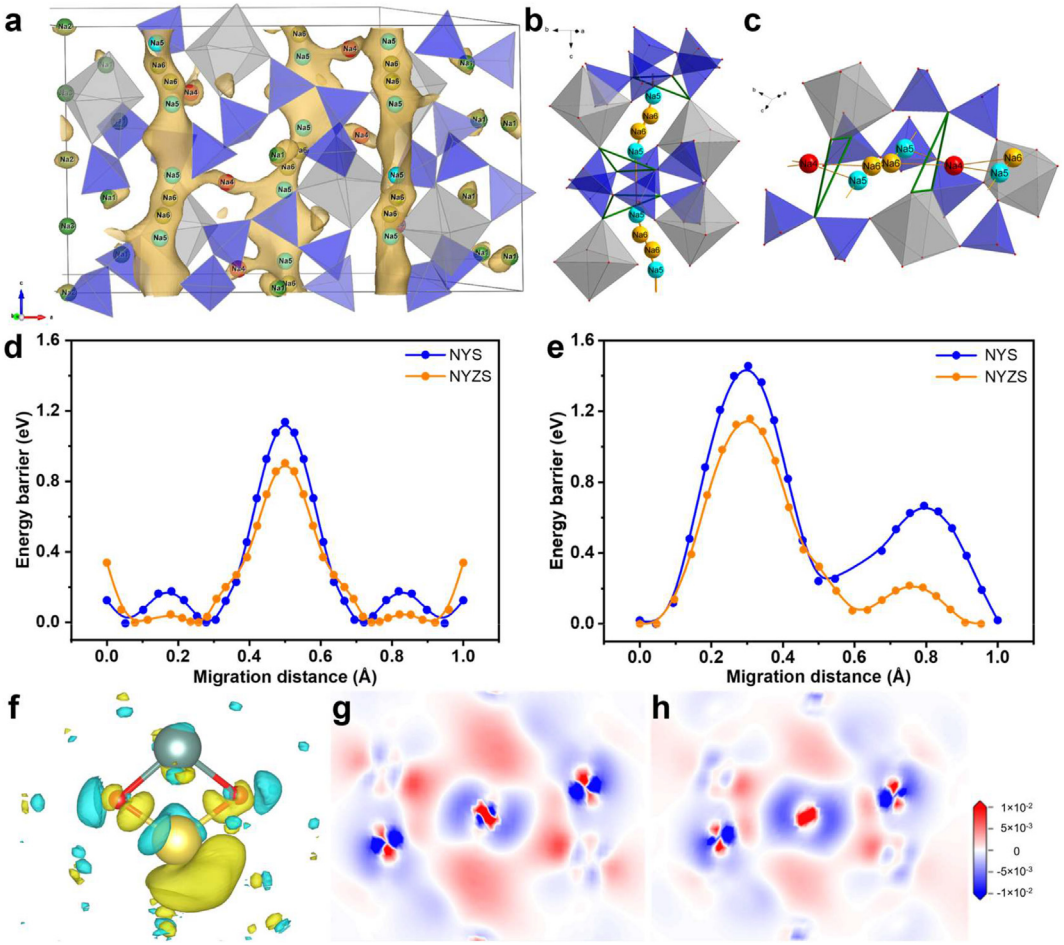

Fig. 4. Simulation results for NYS and NYZS. (a) The two distinct transport pathways within NYZS are revealed by the BVSE method. The vertical channels represent 1D channels 5-6-5, in which the Na^+ ions diffuse along the *c* axis. Besides, the horizontal channels between adjacent 5-6-5 channels represent channels 5(6)-4-5(6). The 3D Na^+ ion diffusion network is based on the two perpendicular channel systems. The magnified diffusion pathways are shown in (b) channel 5-6-5 and (c) 5(6)-4-5(6). The energy barriers for Na^+ ion diffusion along (d) channel 5-6-5 and (e) channel 5(6)-4-5(6) of both samples reveal lower energy barriers in NYZS. (f) The slices of charge difference of Na between (g) NYZS and (h) NYS show the lower electronic distribution of Na in NYZS. The inset of the contour plot denotes the intensity of the electronic distribution around Na.

Here, only the minority component, having the higher relaxation rate, is used. The slower motion of the Na^+ ions characterized by a slower relaxation rate is not taken into account. This explains the differences in the E_a compared to the results of the EIS (Fig. 2b).

2.4. Na^+ ion migration pathways

The bond valence site energy (BVSE) method was used to simulate ionic transport pathways. According to the main rule that atomic valence should be equal to the sum of bond valences around the atom, the two distinct transport pathways that are accessible for mobile Na^+ ions can be obtained, as shown in Fig. 4a. Na5 can migrate to the next periodical sites through Na6 to form 1D diffusion channels along the *c* axis, denoted as 5-6-5 (Fig. 4b). These channels of 5-6-5 are connected by Na4 sites with zigzag chains, denoted as 5(6)-4-5(6) (Fig. 4c), and a 3D network for Na^+ ion diffusion forms within the NYZS crystal framework. Based on the results of density functional theory (DFT) simulation, the transport energy barriers of Na^+ ions along 5-6-5 and 5(6)-4-5(6) in NYS are 1.2 (Fig. 4d) and 1.5 eV (Fig. 4e), respectively, while the energy barriers are decreased to 0.9 and 1.1 eV in NYZS. The results indicate that Zr^{4+} substitution plays a crucial role in the enhanced conductivity of NYZS, and channel 5-6-5 is the main pathway for Na^+ ion diffusion. To further clarify the contribution of Zr^{4+} substitution to the decrease of the diffusion energy barrier, the charge difference profile that a Na^+ ion experiences when crossing the bottleneck of channel 5-6-5 was calculated. The slices are fixed on the plane of the Na, Y/Zr and their adjacent O atoms (Fig. 4f), in which more charges are delocalized around the Na in NYZS (Fig. 4g) than in NYS (Fig. 4h), which are attributed to the stronger electrophilicity of Zr than that of Y resulting from the different electronegativity and resulting in a stronger Zr–O bond than Y–O bond. The decreased charges around Na are associated with decreased Na–O bond strength and increased mobility and contribute to the enhanced conductivity of NYZS, which is also revealed from the 2D ^{23}Na MQ MAS NMR profiles and the evolved chemical environment after Zr^{4+} substitution.

2.5. Comparison with other investigations on NYS and other oxide-based Na^+ ionic SSEs

The reports with the most conductive NYS examples are those dealing with single-crystalline materials and revealing ionic conductivities of 5–7 mS cm^{-1} at RT [33] (Fig. 5a). Polycrystalline NYS usually shows up to one order of magnitude lower conductivities [34,35]. The NYS investigated here presents one of the highest $\sigma_{total\text{-}RT}$ values (1.3 mS cm^{-1}), comparable with conductivities obtained for NYS tape [14] or pellet [25] (1–1.5 mS cm^{-1}). Formerly, the substitutions of Y with rare

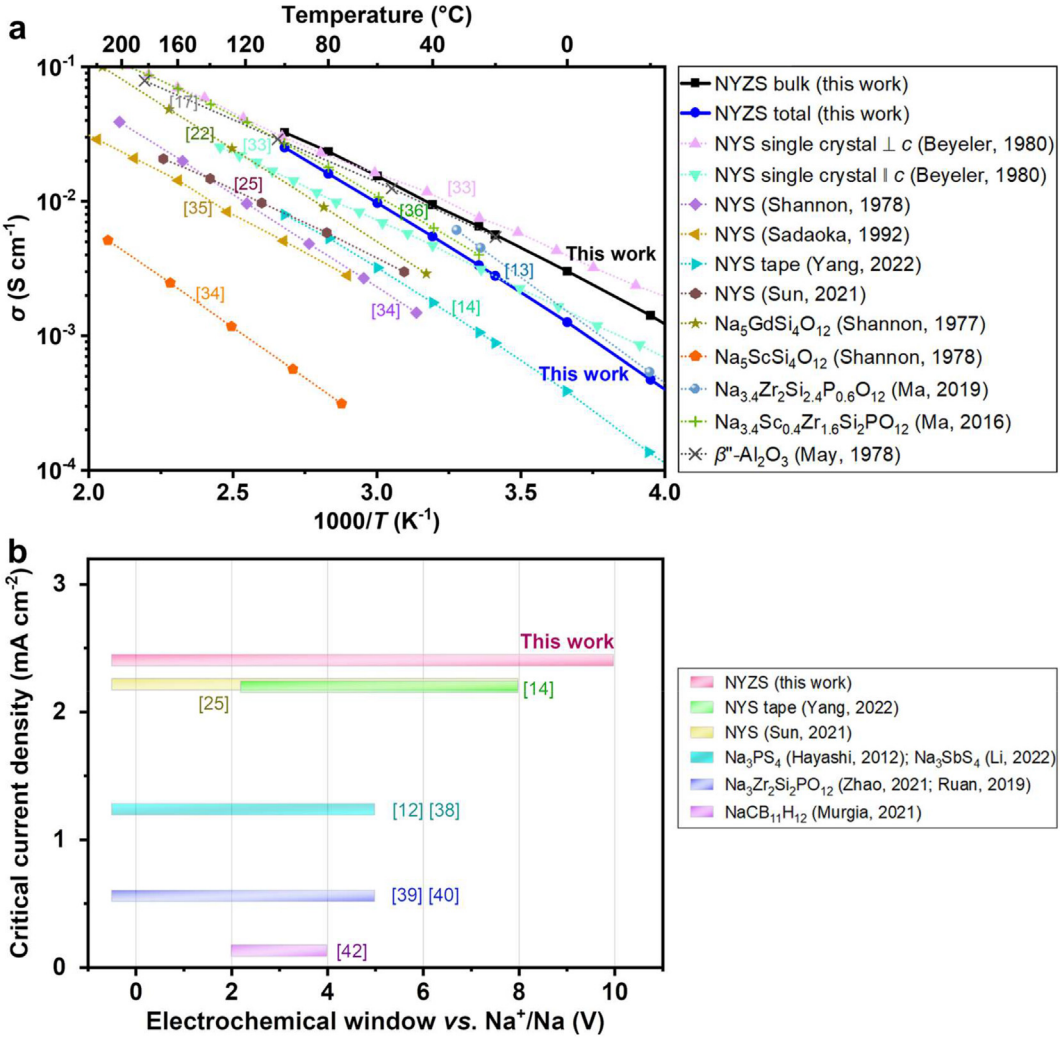

Fig. 5. Comparison of electrical conductivity and electrochemical stability between NYZS and reported representative Na^+ ionic SSEs. (a) The Arrhenius plots of NYS single crystal (perpendicular and parallel to *c* axis) [33], polycrystalline NYS [25,34,35], NYS tape [14], $Na_5GdSi_4O_{12}$ [22], $Na_5ScSi_4O_{12}$ [34], $Na_{3.4}Zr_2Si_{2.4}P_{0.6}O_{12}$ [13,37], $Na_{3.4}Sc_{0.4}Zr_{1.6}Si_2PO_{12}$ [36], β''-Al_2O_3 [17], NYZS with bulk and total conductivities. (b) The integrated comparison of critical current density and electrochemical windows of NYS tape [14], NYS pellet [25], Na_3PS_4 [12], Na_3SbS_4 [38], $Na_3Zr_2Si_2PO_{12}$ [39–41], $NaCB_{11}H_{12}$ [42] and NYZS at RT.

earth elements showed an influence on conductivity [22,34], but the aliovalent substitution with Zr and the increase of sodium vacancies seem to have a more substantial impact on the improvement of the ionic transport. In the case of NYZS, the ionic conductivity is significantly increased to 3.3 mS cm^{-1} and is already comparable to the extensively studied NASICON materials (e.g., $Na_{3.4}Zr_2Si_{2.4}P_{0.6}O_{12}$ [13], $Na_{3.4}Sc_{0.4}Zr_{1.6}Si_2PO_{12}$ [36]) and β''-Al_2O_3 [17]. In addition, it is worth mentioning that the bulk conductivity of NYZS exactly coincides with the single-crystal measurement of Beyeler *et al.* [33] and the $\sigma_{bulk\text{-}RT}$ is as high as 6.5 mS cm^{-1}. The detailed data are listed in Supplementary Table S10.

In addition to superior σ and typical E_a for Na^+ ion conduction, the electrochemical stability window and the CCD are parameters determining the electrochemical stability of the materials (shown in Fig. 5b) to be used as SSEs. The detailed information is listed in Supplementary Table S11. Both NYZS and NYS tape/pellet [14,25] have good electrochemical windows, particularly NYZS exhibits the widest electrochemical window between −0.5 and 10 V, which indicates the high voltage endurance of NYZS, far superior to sulfides [12,38] and hydrides [42], etc. NYZS reaches a high CCD of 2.4 mA cm^{-2} at RT, one of the highest values for oxide-based Na^+ ionic conductors (without interfacial treatment), exhibiting good Na dendrite tolerance.

3. Conclusion

In summary, a novel Na^+ ionic conductor NYZS is reported for the first time and shows high bulk and total conductivities up to 6.5 and 3.3 mS cm^{-1}, respectively. The crystallographic structure and the electrical properties of NYZS are thoroughly studied. By using a facile solid-state reaction approach, the resulting NYZS electrolyte allows high densification (> 95% of relative density), excellent phase purity (~96%) and fine grains. From the Rietveld refinement against SYXRD data, the crystal structure and parameters are determined with the space group of $R\bar{3}c$. NYZS is characterized by SiO_4 tetrahedra forming puckered $Si_{12}O_{36}$ rings parallel to the *c* axis. Together with MO_6 (M = Y, Zr) octahedra, these puckered rings form a framework containing two channels in the crystal structure, which are filled by mobile Na^+ ions. It is worth mentioning that NYZS exhibits good environmental stability, with its composition remaining stable and its conductivity not decreasing significantly after three months of exposure to air. The combination of solid-state NMR techniques and theoretical calculations demonstrates that Na^+ ions have a three-dimensional transportation pathway in NYZS. It also reveals a synergistic effect of increased vacancies and the improved chemical environment with Zr^{4+} substitution, which explains the origin of the high conductivity and low activation energy. Considering the simple synthesis method, ultra-high stability and excellent electrochemical properties, NYZS is a very promising SSE for large-scale SSSBs operating at RT.

4. Experimental section

4.1. Materials preparation

NYS and $Na_{5-x}Y_{1-x}Zr_xSi_4O_{12}$ powders (with different Zr substitutions of 0.04, 0.06, 0.08, 0.10, 0.12, 0.14, 0.2, 0.4, 0.6, 0.8, 1.0 mol) were prepared by solid-state reaction. All the starting materials, $Na_2CO_3{\cdot}H_2O$ (Alfa Aesar, 99.5%), Y_2O_3 (MaTeck, 99.999%), SiO_2 (Aldrich) and ZrO_2 (Alfa Aesar, 99+%), were mixed stoichiometrically and put into a polyethylene vial (250 ml) with zirconia balls (200 g milling balls with diameters of 3 and 5 mm) as grinding agent and ethanol (150 ml) as the dispersant. The ball milling time was 48 h. Before mixing the starting materials, Y_2O_3 and ZrO_2 powders were heated at 900 °C for 3 h to remove the moisture. After ball-mixing the powders, the white slurry was put out and dried in an oven at 60 °C for 10 h. Then, the white powders were calcined at 500 °C for 5 h in air before pressing to remove gaseous residuals and get dense pellets. In the calcination process, there is no phase formation or crystallization. After calcination, the powders were uniaxially pressed into pellets (Ø = 13 mm) with a pressure of 100 MPa and sintered at 1100 °C for 6 h in air.

4.2. Structural characterization

Synchrotron X-ray diffraction experiments were measured with powder sample NYZS in a 0.8 mm diameter glass capillary (WJM) at the beamline of PETRA III beamline P02.1 at the Deutsches Elektronen-Synchrotron (DESY). Wavelength for the measurement was λ = 0.207349 Å and the integration time for the sample was 300 s. The sample was spun during the measurement for obtaining better statistics. The area detector was a Varex XRD 4343CT (150 × 150 μm^2 pixel size and 2880 × 2880 pixel area with a CsI scintillator directly deposited on amorphous Si photodiodes). Data were integrated using the DAWN Science Software [43]. The data were analyzed with the Rietveld method by using the General Structure Analysis System (GSAS) [44]. Temperature-dependent XRD patterns were characterized by powder X-ray diffraction (D4, Bruker) with Cu K_α radiation. The morphology was characterized by scanning electron microscopy (SEM, S-4800) equipped with energy-dispersive X-ray spectroscopy and high-resolution transmission electron microscopy (HRTEM, 2100F). The surface oxidation and the composition were confirmed by X-ray photoelectron spectroscopy (XPS, PHI-5300 ESCA 1610 SAM).

4.3. Electrochemical characterizations

The electrochemical performances (impedance spectroscopy, galvanostatic cycling profiles, DC polarization and cyclic voltammetry (CV)) were tested with a Biologic multi-channel electrochemical workstation (VMP 300) and a combined electrochemical system (Keysight E4991B and Novocontrol Technologies Alpha-A). These electrochemical data were recorded at RT unless otherwise specified. All tested cells were assembled in the Ar-filled glovebox (Glovebox System, Germany) with Swagelok cell models or pouch-type cells. The sandwich-structured cells were assembled for the AC impedance measurements by attaching Na foils or sputtering Au coatings on both sides of the as-prepared pellets. The testing frequency ranges were from 3 GHz or 7 MHz to 1 Hz applying an amplitude of 5 mV. The galvanostatic cycling performance was tested with Na/NYZS/Na symmetric cells at the current density of 1 mA cm^{-2} and the deposition capacity of 1 mAh cm^{-2} every half cycle. Preparation of the Super P electrode and (Super P + NYZS) composite electrode followed the routine procedure but with different ratios [24]. For both electrodes, polyvinylidenfluorid (PVDF, M_w = 600,000, Sigma-Aldrich) with a ratio of 10 wt% was used as the binder. For the composite electrode, the ratio NYZS : Super P was 70 : 20 wt%. The formulation of the liquid electrolyte (LE) was 1.0 M $NaPF_6$ in propylene carbonate (PC), which was purchased from Suzhou Fosai New Material Co., Ltd. The CV curves were measured at different voltage intervals in the cell configuration of Na/NYZS/Au, Na/NYZS/(NYZS + Super P), Na/LE/Super P and Na/LE/(NYZS + Super P) with different scanning speeds.

4.4. NMR measurements

Static ^{23}Na relaxometry and line shape analysis was performed on a Bruker Avance Neo 200 MHz spectrometer at a magnetic field strength of 4.7 T. The samples were sealed in 10 mm evacuated silica glass tubes. The data were acquired with an inversion-recovery and solid-echo pulse sequence in the temperature range from 260 to 595 K. The recycle delay was set to values between 0.4 and 2 s and was always well above $5{\cdot}T_1$. 1 M NaCl was used as a reference for the ^{23}Na NMR spectra.

^{23}Na and ^{29}Si MAS spectra were detected on a 500 MHz Bruker Avance spectrometer using a 2.5 mm rotor at a spinning speed of 30 kHz. The ^{23}Na spectra were referenced with 1 M NaCl and ^{29}Si spectra with tetramethylsilane (TMS). The recycle delays were set to 30 s for the ^{23}Na and 60 s for the ^{29}Si spectra acquisition.

^{89}Y MAS spectra were detected on a Bruker Neo 600 MHz spectrometer (Larmor frequency of 29.42 MHz) using a 7 mm rotor at a spinning speed of 5 kHz. Between 1800 and 2000 scans were acquired for each sample with a relaxation delay of 50 s. The spectra were referenced with respect to the signal of TMS (absolute referencing).

^{23}Na MQMAS NMR experiments were performed on a Bruker Avance III 400 MHz spectrometer using a 2.5 mm rotor at a spinning speed of 25 kHz. Two-dimensional ^{23}Na MQMAS experiments were performed using a phase-modulated split-t_1 pulse sequence [45,46] with rotor synchronization. A total of 512 t_1 increments were acquired in the F1 dimension, expanded after Fourier transformation to 1024 points.

4.5. Theoretical calculation and fitting methods

All simulations employed the CASTEP and the plane-wave DFT code with generalized gradient approximation (GGA) and Perdew-Burke-Ernzerhof (PBE) exchange functions. The transit search (TS) method was used with the complete linear synchronous transit/quadratic synchronous transit (LST/QST) method. The plane-wave energy cutoff was 500 eV. The core electrons were treated by an ultrasoft pseudopotential. The *k*-point grid was automatically generated with the Monkhorst-Pack method. The simulated results were visualized by VESTA. The BVSE calculations are performed using Fullprof Suite software and isosurfaces of mobile Na^+ ions are displayed by the VESTA visualization package. Impedance data were fitted using the Zview software, Scribner Associates Inc.

Author contributions

Q.M., F.T., J.C. and O.G. supervised the research. A.Y. prepared the samples, tested their electrochemical properties, formalized and wrote the manuscript. K.Y., E.D., and S.Z. did the calculation work and wrote the section. M.S., H.L., I.M. and S.I. performed all the solid-state nuclear magnetic resonance measurements, analyzed the results and M.S. wrote this section. E.D., Q.Z., H.S. and Q.P. conducted the crystallographic analysis. M.E. conducted synchrotron X-ray diffraction measurement and analyzed the results together with X.S. Q.L., R.Y. participated in the discussion of the results and Q.L. measured the X-ray photoelectron spectroscopy. X.W. conducted scanning electron microscopy, transmission electron microscopy, X-ray photoelectron spectroscopy and analyzed them. All the authors contributed to the results, analysis, discussion, and have approved the final version of the manuscript.

Declaration of competing interest

The authors declare no competing financial interests.

Acknowledgments

A.Y., H.L. and Q.L. gratefully acknowledge the China Scholarship Council (CSC, Grant Nos. 201906200023, 201906200016 and 201808080137, respectively) for financial support. A.Y., whose CSC grant application is affiliated with Nankai University (Tianjin, China), would like to express his deep gratitude to the Key Laboratory of Advanced Energy Materials Chemistry (AEMC) at Nankai University. The authors appreciate the help from Dr. Yoo Jung Sohn for the measurement of temperature-dependent XRD and Mr. Volker Bader for the heat treatments. We acknowledge DESY (Hamburg, Germany), a member of the Helmholtz Association HGF, for the provision of experimental facilities. Parts of this research were carried out at PETRA III beamline P02.1. Beamtime was allocated by an In-House contingent. X.S. acknowledges funding from the European Union's Horizon 2020 research, innovation program under the Marie Sklodowska-Curie grant agreement (No. 101034329) and the WINNINGNormandy Program supported by the Normandy Region, France. The authors take responsibility for the content of this publication.

Appendix A. Supplementary data

Supplementary data to this article can be found online at https://doi.org/10.1016/j.esci.2023.100175.

References

[1] C. Bauer, S. Burkhardt, N.P. Dasgupta, L.A.-W. Ellingsen, L.L. Gaines, H. Hao, R. Hischier, L. Hu, Y. Huang, J. Janek, C. Liang, H. Li, J. Li, Y. Li, Y.-C. Lu, W. Luo, L.F. Nazar, E.A. Olivetti, J.F. Peters, J.L.M. Rupp, M. Weil, J.F. Whitacre, S. Xu, Charging sustainable batteries, Nat. Sustain. 5 (2022) 176–178.
[2] H. Li, Practical evaluation of Li-ion batteries, Joule 3 (2019) 911–914.
[3] M. Li, J. Lu, Z. Chen, K. Amine, 30 years of lithium-ion batteries, Adv. Mater. 30 (2018) e1800561.
[4] Y. Lu, J. Chen, Prospects of organic electrode materials for practical lithium batteries, Nat. Rev. Chem 4 (2020) 127–142.
[5] Y. Sun, X. Wang, A. Yang, Y. Huang, W. Jia, D. Jia, F. Cheng, M. Xu, M. Li, Y. Lu, Functional separator with a lightweight carbon-coating for stable, high-capacity organic lithium batteries, Chem. Eng. J. 418 (2021) 129404.
[6] X. Wang, Z. Shang, A. Yang, Q. Zhang, F. Cheng, D. Jia, J. Chen, Combining quinone cathode and ionic liquid electrolyte for organic sodium-ion batteries, Chem 5 (2019) 364–375.
[7] Y. Lu, L. Li, Q. Zhang, Z. Niu, J. Chen, Electrolyte and interface engineering for solid-state sodium batteries, Joule 2 (2018) 1747–1770.
[8] Y.-F. Zhu, Y. Xiao, S.-X. Dou, Y.-M. Kang, S.-L. Chou, Spinel/post-spinel engineering on layered oxide cathodes for sodium-ion batteries, eScience 1 (2021) 13–27.
[9] A. Yang, X. Wang, Y. Lu, L. Miao, W. Xie, J. Chen, Core-shell structured 1,4-benzoquinone@TiO_2 cathode for lithium batteries, J. Energy Chem. 27 (2018) 1644–1650.
[10] Y. Guo, S. Wu, Y.-B. He, F. Kang, L. Chen, H. Li, Q.-H. Yang, Solid-state lithium batteries: safety and prospects, eScience 2 (2022) 138–163.
[11] Q. Lu, A. Yang, A. Omar, Q. Ma, F. Tietz, O. Guillon, D. Mikhailova, Recent advances in stabilization of sodium metal anode in contact with organic liquid and solid-state electrolytes, Energy Technol. 10 (2022) 2200149.
[12] A. Hayashi, K. Noi, A. Sakuda, M. Tatsumisago, Superionic glass-ceramic electrolytes for room-temperature rechargeable sodium batteries, Nat. Commun. 3 (2012) 856.
[13] Q. Ma, C.-L. Tsai, X.-K. Wei, M. Heggen, F. Tietz, J.T.S. Irvine, Room temperature demonstration of a sodium superionic conductor with grain conductivity in excess of 0.01 S cm^{-1} and its primary applications in symmetric battery cells, J. Mater. Chem. A 7 (2019) 7766–7776.
[14] A. Yang, R. Ye, X. Li, Q. Lu, H. Song, D. Grüner, Q. Ma, F. Tietz, D. Fattakhova-Rohlfing, O. Guillon, Fabrication of thin sheets of the sodium superionic conductor $Na_5YSi_4O_{12}$ with tape casting, Chem. Eng. J. 435 (2022) 134774.
[15] B. Tang, Y. Zhao, Z. Wang, S. Chen, Y. Wu, Y. Tseng, L. Li, Y. Guo, Z. Zhou, S.-H. Bo, Ultrathin salt-free polymer-in-ceramic electrolyte for solid-state sodium batteries, eScience 1 (2021) 194–202.
[16] Y. Lu, L. Li, Q. Zhang, Y. Cai, Y. Ni, J. Chen, High-performance all-solid-state electrolyte for sodium batteries enabled by the interaction between the anion in salt and Na_3SbS_4, Chem. Sci. 13 (2022) 3416–3423.
[17] G.J. May, A. Hooper, The effect of microstructure and phase composition on the ionic conductivity of magnesium-doped sodium-beta-alumina, J. Mater. Sci. 13 (1978) 1480–1486.
[18] Q. Ma, T. Ortmann, A. Yang, D. Sebold, S. Burkhardt, M. Rohnke, F. Tietz, D. Fattakhova-Rohlfing, J. Janek, O. Guillon, Enhancing the dendrite tolerance of NaSICON electrolytes by suppressing edge growth of Na electrode along ceramic surface, Adv. Energy Mater. 12 (2022) 2201680.
[19] H.Y.-P. Hong, Crystal structures and crystal chemistry in the system $Na_{1+x}Zr_2Si_xP_{3-x}O_{12}$, Mater. Res. Bull. 11 (1976) 173–182.
[20] X. Liu, Q. Lu, A. Yang, Y. Qian, High ionic conductive protection layer on Zn metal anode for enhanced aqueous zinc-ion batteries, Chin. Chem. Lett. 34 (2022) 107703.
[21] B.A. Maksimov, Y.A. Kharitonov, N.V. Belov, Crystal structure of the Na-Y metasilicate $Na_5YSi_4O_{12}$, Sov. Phys. Dokl. 18 (1974) 763–765.
[22] R.D. Shannon, H.-Y. Chert, T. Berzins, Ionic conductivity in $Na_5GdSi_4O_{12}$, Mater. Res. Bull. 12 (1977) 969–973.
[23] H.U. Beyeler, T. Hibma, The sodium conductivity paths in the superionic conductors $Na_5RESi_4O_{12}$, Solid State Commun. 27 (1978) 641–643.
[24] A. Yang, R. Ye, H. Song, Q. Lu, X. Wang, E. Dashjav, K. Yao, D. Grüner, Q. Ma, F. Tietz, O. Guillon, Pressureless all-solid-state Na/S batteries with self-supporting $Na_5YSi_4O_{12}$ scaffolds, Carbon Energy (2023), https://doi.org/10.1002/cey2.371.
[25] G. Sun, X. Yang, N. Chen, S. Yao, X. Wang, X. Jin, G. Chen, Y. Xie, F. Du, $Na_5YSi_4O_{12}$: a sodium superionic conductor for ultrastable quasi-solid-state sodium-ion batteries, Energy Stor. Mater. 41 (2021) 196–202.
[26] J.T.S. Irvin, D.C. Sinclair, A.R. West, Electroceramics: characterization by impedance spectroscopy, Adv. Mater. 2 (1990) 132–138.
[27] K. Takada, Progress in solid electrolytes toward realizing solid-state lithium batteries, J. Power Sources 394 (2018) 74–85.
[28] F. Han, Y. Zhu, X. He, Y. Mo, C. Wang, Electrochemical stability of $Li_{10}GeP_2S_{12}$ and $Li_7La_3Zr_2O_{12}$ solid electrolytes, Adv. Energy Mater. 6 (2016) 1501590.
[29] Y. Tian, T. Shi, W.D. Richards, J. Li, J.C. Kim, S.-H. Bo, G. Ceder, Compatibility issues between electrodes and electrolytes in solid-state batteries, Energy Environ. Sci. 10 (2017) 1150–1166.

[30] V. Lacivita, Y. Wang, S.-H. Bo, G. Ceder, Ab initio investigation of the stability of electrolyte/electrode interfaces in all-solid-state Na batteries, J. Mater. Chem. A 7 (2019) 8144–8155.
[31] X. Liu, R. Garcia-Mendez, A.R. Lupini, Y. Cheng, Z.D. Hood, F. Han, A. Sharafi, J.C. Idrobo, N.J. Dudney, C. Wang, C. Ma, J. Sakamoto, M. Chi, Local electronic structure variation resulting in Li 'filament' formation within solid electrolytes, Nat. Mater. 20 (2021) 1485–1490.
[32] C. Wang, T. Deng, X. Fan, M. Zheng, R. Yu, Q. Lu, H. Duan, H. Huang, C. Wang, X. Sun, Identifying soft breakdown in all-solid-state lithium battery, Joule 6 (2022) 1770–1781.
[33] H.U. Beyeler, R.D. Shannon, H.Y. Chen, Ionic conductivity of single-crystal $Na_5YSi_4O_{12}$, Appl. Phys. Lett. 37 (1980) 934–935.
[34] R.D. Shannon, B.E. Taylor, T.E. Gier, H.-Y. Chen, T. Berzins, Ionic conductivity in $Na_5YSi_4O_{12}$-type silicates, Inorg. Chem. 17 (1978) 958–964.
[35] Y. Sadaoka, M. Matsuguchi, Y. Sakai, K. Komatsubara, Ionic conductivity in $Na_5YSi_4O_{12}$-based ceramics with and without additives, J. Mater. Sci. 27 (1992) 5045–5051.
[36] Q. Ma, M. Guin, S. Naqash, C.-L. Tsai, F. Tietz, O. Guillon, Scandium-substituted $Na_3Zr_2(SiO_4)_2(PO_4)$ prepared by a solution-assisted solid-state reaction method as sodium-ion conductors, Chem. Mater. 28 (2016) 4821–4828.
[37] Z. Deng, T.P. Mishra, E. Mahayoni, Q. Ma, A.J.K. Tieu, O. Guillon, J.N. Chotard, V. Seznec, A.K. Cheetham, C. Masquelier, G.S. Gautam, P. Canepa, Fundamental investigations on the sodium-ion transport properties of mixed polyanion solid-state battery electrolytes, Nat. Commun. 13 (2022) 4470.
[38] L. Li, R. Xu, L. Zhang, Z. Zhang, M. Yang, D. Liu, X. Yan, A. Zhou, O-tailored microstructure-engineered interface toward advanced room temperature all-solid-state Na batteries, Adv. Funct. Mater. 32 (2022) 2203095.
[39] Y. Ruan, F. Guo, J. Liu, S. Song, N. Jiang, B. Cheng, Optimization of $Na_3Zr_2Si_2PO_{12}$ ceramic electrolyte and interface for high performance solid-state sodium battery, Ceram. Int. 45 (2019) 1770–1776.
[40] Y. Zhao, C. Wang, Y. Dai, H. Jin, Homogeneous Na^+ transfer dynamic at Na/$Na_3Zr_2Si_2PO_{12}$ interface for all solid-state sodium metal batteries, Nano Energy 88 (2021) 106293.
[41] Z. Zhang, S. Wenzel, Y. Zhu, J. Sann, L. Shen, J. Yang, X. Yao, Y.-S. Hu, C. Wolverton, H. Li, L. Chen, J. Janek, $Na_3Zr_2Si_2PO_{12}$: a stable Na^+-ion solid electrolyte for solid-state batteries, ACS Appl. Energy Mater. 3 (2020) 7427–7437.
[42] F. Murgia, M. Brighi, L. Piveteau, C.E. Avalos, V. Gulino, M.C. Nierstenhofer, P. Ngene, P. de Jongh, R. Cerny, Enhanced room-temperature ionic conductivity of $NaCB_{11}H_{12}$ via high-energy mechanical milling, ACS Appl. Mater. Interfaces 13 (2021) 61346–61356.
[43] J. Filik, A.W. Ashton, P.C.Y. Chang, P.A. Chater, S.J. Day, M. Drakopoulos, M.W. Gerring, M.L. Hart, O.V. Magdysyuk, S. Michalik, A. Smith, C.C. Tang, N.J. Terrill, M.T. Wharmby, H. Wilhelm, Processing two-dimensional X-ray diffraction and small-angle scattering data in DAWN 2, J. Appl. Crystallogr. 50 (2017) 959–966.
[44] B.H. Toby, EXPGUI, a graphical user interface for GSAS, J. Appl. Crystallogr. 34 (2001) 210–213.
[45] S.P. Brown, S. Wimperis, Two-dimensional multiple-quantum MAS NMR of quadrupolar nuclei. Acquisition of the whole echo, J. Magn. Reson. 124 (1997) 279–285.
[46] S.P. Brown, S. Wimperis, Two-dimensional multiple-quantum MAS NMR of quadrupolar nuclei: a comparison of methods, J. Magn. Reson. 128 (1997) 42–61.